

# Atmospheric

## 17. Atmospheric Measurements

A selected group of common instruments used to measure the atmosphere is described in this chapter. Typical atmospheric measurements include winds, temperature, pressure, humidity, dew point, moisture, radiation, visibility, cloud heights, lightning, gaseous composition, aerosols, and precipitation. Atmospheric sensors may measure at a point (in space) or remotely (with a given distance from the volume of air being measured). As an example of a common wind sensor, sonic anemometers measure wind speed in two or three directions using differences in the propagation speed of sound in different directions across moving air. The surface heat budget, e.g., solar radiation, albedo, the Earth's long-wave radiation, heat fluxes into the soil, and latent/sensible heat fluxes are major forcing effects for atmospheric motions. Standard measurement methodologies are presented in Sect. 17.1.3. Some of the most frequently used measuring instruments for atmospheric dispersion are reviewed in Sect. 17.2. Major field experiments have recently used arrays of both *bag* samplers and fast response sensors to track the dispersion of plumes of trace gases in urban areas. Remote sensing instruments, both active and passive, are becoming increasingly available and robust. Remote sensing instruments may

17.1	<b>Point Measurements</b> .....	1159
17.1.1	Wind Velocity.....	1159
17.1.2	Temperature, Relative Humidity, and Pressure .....	1162
17.1.3	Fluxes.....	1164
17.1.4	Vertical Profiling .....	1166
17.2	<b>Dispersion Measurements</b> .....	1167
17.2.1	Tracers .....	1167
17.2.2	Bag Samplers.....	1168
17.2.3	Fast-Response Sensors.....	1168
17.2.4	Recent Major Field Experiments .....	1168
17.3	<b>Remote Sensing</b> .....	1169
17.3.1	Lidar.....	1169
17.3.2	Ceilmeters .....	1172
17.3.3	Sodar.....	1172
17.3.4	Radar Profilers .....	1174
17.3.5	RASS .....	1174
17.4	<b>Satellite Measurements</b> .....	1175
	<b>References</b> .....	1178

be ground-based or satellite based. While the flexibility and power of modern remote sensing instruments is impressive, there is frequently an inversion challenge associated with data interpretation.

Measurement of atmospheric flow and airborne material at different scales and with varying space-time resolutions is of great utility for meteorologists, atmospheric physicists, communication engineers, military planners, and teams subjected to major technological risks. Low space-time-resolution atmospheric data are used for forecasting and emergency planning, whereas high-resolution data are employed in atmospheric flow and dispersion research. Typical atmospheric measurements include winds, temperature, pressure, humidity, dew point, moisture, radiation, visibility, cloud heights, lightning, gaseous composition (e.g., CO<sub>2</sub>, pollutants), aerosols, and precipitation. Over the past few decades, major technological advances have been made with regard to atmospheric sensors (detectors) as well as

sensor platforms (which support a battery of sensors such as satellites, aircraft and towers). The advent of *fast-response* (typically up to 100 Hz) and *mean-value* sensors for direct and remote sensing measurements and progress in data acquisition, calibration, management, analysis, and quality-assurance techniques have enabled measurements with ever-increasing reliability and accuracy. Direct sensors make in situ measurements at a given location whereas remote sensors measure wave signals that are generated or modified by atmospheric phenomena at some distance away. The remote sensors that emit a particular type of waves (e.g., sound, light, microwaves) from a transmitter and receive the modified signal at a receiver are called *active* remote sensors whereas those that capitalize on receiving stray

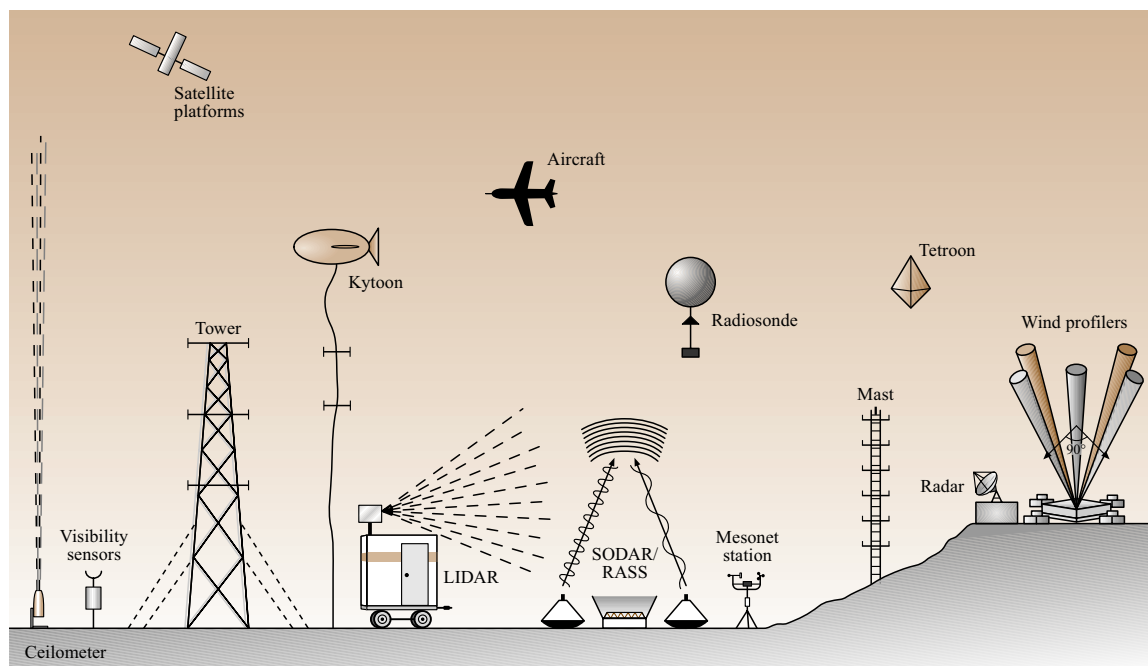


**Fig. 17.1** A schematic of an atmospheric flow sensor deployment in a field campaign

waves emitted or reflected by atmospheric constituents or the Earth's surface are called passive remote sensors. Direct sensors have high space–time resolution, but they may also modify local wind fields to yield potentially unrepresentative point values. Remote sensing offers wide-area coverage (sometimes over periods of many years with the same instrumentation, as in the case of satellites) and physically nonintrusive measurements that are often more cost-effective than surface instruments, but usually their spatial resolution is limited, their view may be obscured by the clouds and gasses, and they may require convoluted calibration techniques.

Figure 17.1 shows a schematic of an idealized field campaign with an array of atmospheric instruments and instrument platforms. The meteorological mast, with a typical height of 10–50 m, is used to place point instruments at various heights. Sometimes much higher permanent masts (e.g., 300 m in Boulder, and 213 m in Cabauw) are used. Instruments associated with masts include: sensors for wind velocity (e.g., sonic, cup, hot-wire and vane anemometers), refractive index (scintillometers), visibility (transmissometers, backscatter meters, cameras, nephelometers) and falling precipitation (disdrometer); thermometers (thermistors, thermocouples); barometers (aneroid and capacitive elements); hygrometers (hygristors, psychrometers);

rain/snow gauges (bucket and electrically heated gauges, snowboards and pillows); and radiometers (net radiometers, pyranometers, pyrheliometers, diffusometers and pygeometers). Most of these instruments are multi-purpose and measure more than one variable. Smaller portable mesonet stations are also employed, which consist of temperature, humidity, rain, pressure, radiation, and turbulent flux measurements at 2 m and 10 m. The flow around larger towers can be significantly disturbed by the structure, and thus instruments are deployed on booms projecting several meters outward of the tower, directed at different directions with the hope that one of the sensors will be facing the upwind direction.

Kytoons are helium balloons tethered to a winch on the ground. They are portable *towers* with instruments suspended along the tether at different heights. Tethers are available up to  $\approx 2$  km height, although air-traffic restrictions limit their use to less than 800 m, depending on the airspace. They can be used as instrument *towers* at a fixed balloon elevation or as profilers when the balloon is ascending or descending. The use of kytoons is limited because of their limited carrying capacity and difficulties at wind speeds above 5 m/s. Other profiling equipment includes radiosondes or rawinsondes (helium-filled expendable balloons carrying instrument

packages) and tetroons (constant-pressure, balloons with a tetrahedron shape and suspended instruments, which theoretically stay at a constant altitude). Such platforms typically measure temperature, humidity, and pressure information (known as raobs) and are commonly used in operational weather forecasting.

Active remote sensors shown in Fig. 17.1 include radars (radio detection and ranging), sodars, sodars (which employ sound instead of radio waves), lidars (which employ light), and ceilometers (cloud-height measuring devices based on lidar technology). Typically they emit wave pulses, and the time and strength of signal returns allow the calculation of the distance to, and magnitude of, the quantity being measured. They can be used either on the ground or on an aircraft, but their size and large power requirements require the use of larger aircraft. Ground remote sensors can scan vertical swaths at a fixed azimuthal angle called a range–height indicator (RHI) or at a fixed polar angle known as a plan–position indicator (PPI). Volume scans can be obtained using a combination of the two techniques.

## 17.1 Point Measurements

Measurements taken at a fixed point or volume in space are known as point measurements. A typical setup for point measurements consists of a tower equipped with an array of sensors. Some of the quantities of interest are the wind speed and direction, temperature, solar radiation, relative humidity, pressure, and turbulent fluxes. In this section an overview of most commonly used point measurement sensors is given.

### 17.1.1 Wind Velocity

Standard meteorological convention determines the  $U$  wind component along the east–west direction, the  $V$  component along the south–north direction, and the  $W$  component vertically upward (against gravity). Wind direction is given in angular degrees, clockwise from the north (e.g., an easterly wind has a direction of  $90^\circ$ ). Note that some sensor manufacturers use different conventions, based on the instrument axis. If this is the case, one of the first steps in postprocessing and quality control should be correcting for wind direction (and its components) to the standard convention. To measure the mean wind, so-called cup and propeller anemometers are used (Figs. 17.2, 3). Their sampling rate is on the order of one second and data is usually stored as 1–30 min averages. The output is a voltage or frequency (magnet-

A wide range of aircraft platforms are used, including ultralights, gliders, single- and multiengine propeller or turboprop aircraft, helicopters, jets, and cabin-class civilian/military aircraft. The instruments are typically mounted on special booms projecting outside the boundary layer or on special pods to minimize aircraft-induced disturbances. The high speeds (typically 50–100 m/s) of aircraft and limitations of sensor response make it necessary to obtain large space–time segments in order to yield statistically stable turbulence statistics, which is difficult in practice. More recently, satellites have become useful tools for atmospheric observations, with satellite sensors providing routine data with resolution down to a few meters.

A number of point and remote sensors, and sensor platforms are briefly discussed in this chapter. Given the sophistication, complexity, and variety of the available atmospheric sensors and sensor platforms, a comprehensive review of them all is not feasible in such a limited space, and thus only selected commonplace atmospheric flow-measurement tools are described.

activated reed switch), depending on the model, and they are very simple to use in combination with any standard data logger with a voltage or pulse-count input.

These types of anemometers have threshold speed of  $\approx 0.5$  m/s and an accuracy of  $\approx 0.1$  m/s, which is sufficient for routine (operational) meteorological or cli-



**Fig. 17.2**  
The Met-one  
three-cup  
anemometer

matological measurements. Turbulence measurements, however, require higher sampling rates, lower thresholds with higher accuracy, and greater resolution. For this reason cup and propeller anemometers are of limited utility for research-grade measurements.

Sonic anemometers are widely used for wind and temperature measurements. They have superior performance ( $\approx 0.01$  m/s and  $\approx 0.01$  K resolution with  $\approx 0.05$  m/s and  $\approx 0.05$  K accuracy), fast response (up to  $\approx 60$  Hz) and robustness with no moving parts. The electronics are self-contained within the probe, allowing it to be operated as a tower-mounted instrument capable of withstanding hostile environmental conditions. These devices measure the time that an emitted sound wave travels through the air between two ultrasonic transducers (hence the name *sonic*). If the air is in motion, the velocity will influence the speed of sound wave by accelerating or decelerating it. The time of flight of the first emitted signal is equal to

$$t_1 = \frac{s}{c + u_{\text{air}}}, \quad (17.1)$$

and the time of flight of the second signal (emitted from the opposite transducer) is

$$t_2 = \frac{s}{c - u_{\text{air}}}, \quad (17.2)$$

where  $s$ ,  $c$ , and  $u_{\text{air}}$  are the distance between the transducers, the speed of sound, and the wind speed component along the transducers axis, respectively [17.1]. From this information it is straightforward to obtain the along axis wind component  $u_{\text{air}}$  as

$$u_{\text{air}} = \frac{s}{2} \left( \frac{1}{t_1} - \frac{1}{t_2} \right). \quad (17.3)$$

Thus, only the airspeed component along the axis of the ultrasonic transducers is measured. Sonics are equipped with either two (*two-dimensional*) or three (*three-dimensional*) pairs of ultrasonic transducers, which may have orthogonal or nonorthogonal axes. In the latter case, the measured wind speed components are transformed to and expressed as those based on the orthogonal axes. Further, the speed of sound can be found as

$$c = \frac{s}{2} \left( \frac{1}{t_1} + \frac{1}{t_2} \right). \quad (17.4)$$

The speed of sound in moist air is a function of temperature and humidity, which can be written as

$$c^2 = \gamma RT_v, \quad (17.5)$$

where  $\gamma$ ,  $R$ , and  $T_v$  are the ratio of the specific heat of dry air at constant pressure to that at constant volume, the gas constant of dry air, and the virtual air temperature

(the temperature that dry air would have if its pressure and specific volume were the same as a sample of moist air), respectively ( $\gamma = 1.4$ ,  $R = 287.04$  J/(K kg)). In anemometer operation, the virtual temperature is calculated using

$$T_v = \frac{c^2}{\gamma R}. \quad (17.6)$$

If barometric pressure measurements are available independently, the virtual potential temperature can be calculated through

$$\theta_v = \frac{T_v}{\left( \frac{P}{P_0} \right)^{R/c_p}}, \quad (17.7)$$

which is a conserved quantity and is critical for sensible heat flux calculation. Here  $P$ ,  $P_0$ , and  $c_p$  are the pressure, the pressure at the sea level ( $P_0 = 1000$  mbar), and the specific heat at constant pressure, respectively. While most sonic anemometers have comparable accuracy in wind speed measurements, temperature accuracy varies significantly from one make to another, and is reflected in the instrument price. The cheapest sonic anemometers do not even have the capability to measure temperature.

Typically 10 or 20 Hz sampling rates are used for sonics, which is sufficient for turbulence calculations. In postprocessing (which can be performed in real time by a datalogger), the first step is the separation of the mean wind ( $\overline{U}$ ,  $\overline{V}$ ,  $\overline{W}$ , and  $\overline{\theta_v}$ ) from the fluctuating components ( $u'$ ,  $v'$ ,  $w'$ ,  $\theta_v'$ ), selecting a proper averaging period that usually varies from several seconds to several hours, depending on the type of analysis. Additional filtering or trend removal (detrending) techniques may be applied. Fluctuating components are used for the calculations of turbulent intensities in the forms of variances ( $\overline{u'^2}$ ,  $\overline{v'^2}$ , and  $\overline{w'^2}$ ) and Reynolds stresses and fluxes in the forms of covariances ( $\overline{u'v'}$ ,  $\overline{u'w'}$ ,  $\overline{v'w'}$ , and  $\overline{w'\theta_v'}$ ).



**Fig. 17.3** The RM Young propeller anemometer

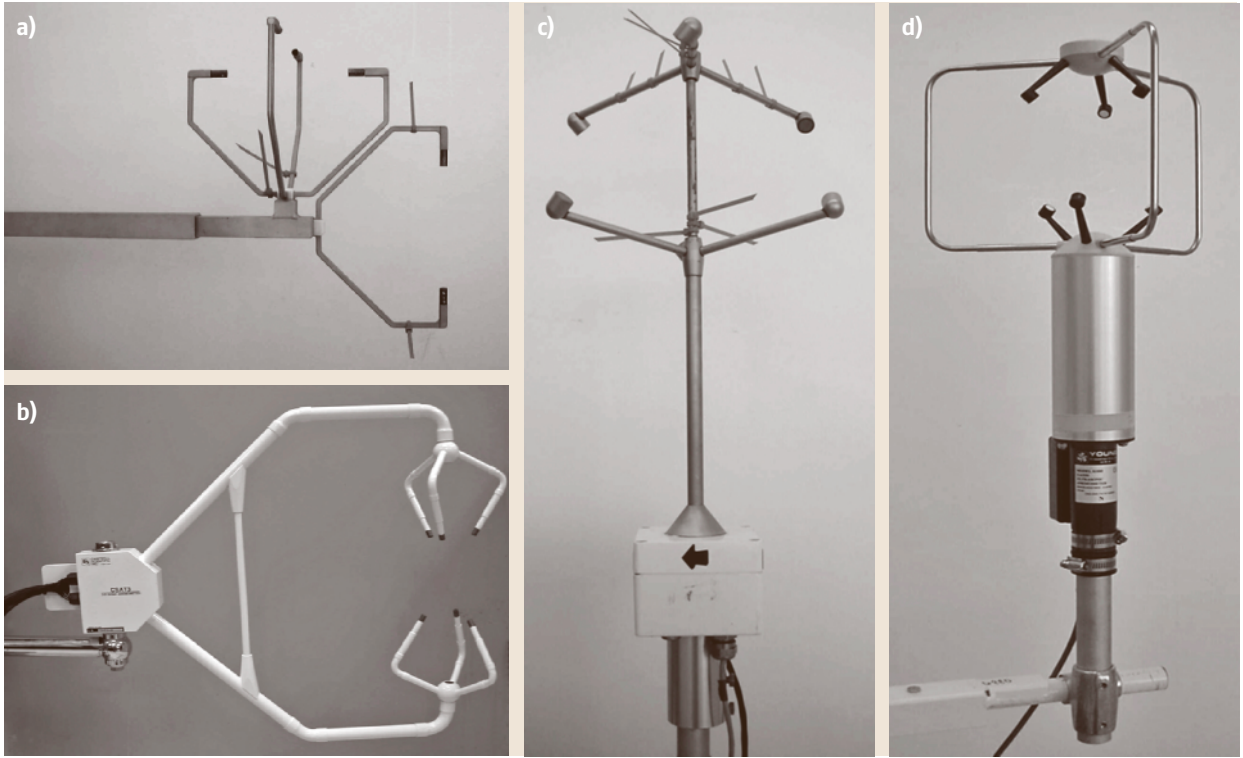


**Fig. 17.4a–d** Sonic anemometers: (a) Applied Technologies Sx, (b) Campbell Scientific CSTAT3, (c) Metek USA 1, (d) RM Young 81000. The wire straps are mounted on the Applied and Metek devices as bird protection – they are recommended for any type of sensor

Three-dimensional sensors have significant advantages over two-dimensional ones, as access to the vertical velocity enables calculations of quantities such as the friction velocity

$$u_* = \sqrt{u'w'^2 + v'w'^2}, \quad (17.8)$$

and the sensible heat flux

$$H_S = \rho c_p \overline{w'\theta'_v}, \quad (17.9)$$

which are crucial for developing atmospheric turbulence parameterizations.

Several sonic anemometer designs exist. For measurements at sites with a prevailing dominant wind direction, probes like those from Applied Technologies Inc. ( $A$ ,  $K$ ,  $S_x$ ,  $V$  and  $V_x$  styles) or the Campbell Sci. CSAT3 probe are usually employed. Careful supporting base designs help minimize flow distortions due to tower interference while permitting a wide unobstructed coverage of the vertical component. These probes are also known for their ability to yield an unobstructed vertical component. Probes such as the

Metek USA1 or RM Young 81 000 allow almost unobstructed measurements of horizontal wind components from any direction, but the supporting base of these types of probes obstructs the vertical wind component. Figure 17.4 shows photographs of these different probe types.

Superior environmental resistance for these probes is achieved by using ultraviolet (UV)-stabilized thermoplastic, stainless-steel, and anodized aluminum components, thereby isolating the sonic anemometer signal from the background noise. Conversely, sonic anemometers do not produce noise that could hamper the operation of nearby instruments, unless ultrasound measurements are made in the proximity of the sonic probe. Sonic probes, however, are not resistant to birds who find sonics arms convenient resting places; to repel them plastic wire straps can be carefully installed without obstructing the instrument operation. Sonics also cannot be operated during rain. Ice on the transducers, which usually occurs in the early morning or when the temperature drops below the freezing point, completely



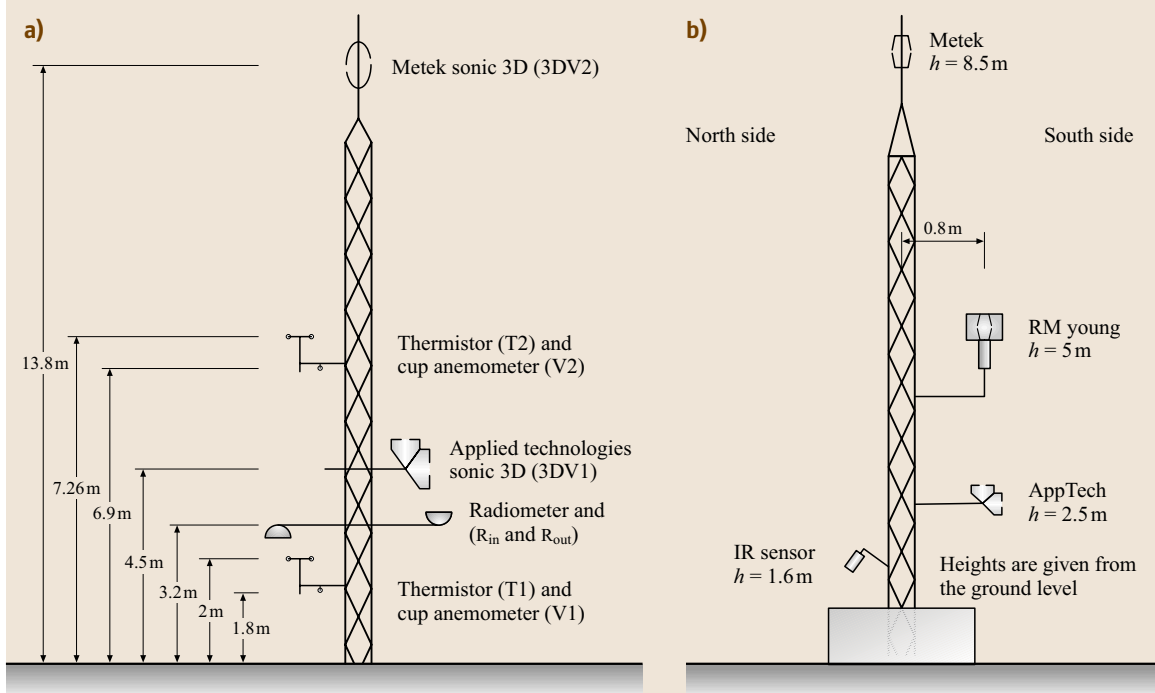


**Fig. 17.5** (a) Schematic of the tower equipped with two sonic anemometers, two cup anemometers, two thermistors, and radiometers used during the VTMX2000 campaign. (b) Tower setup used for the Urban Canyon measurements during the JU2003 campaign. This tower was equipped with three sonic anemometers and an IR sensor for surface temperature measurements

disables the anemometer operation unless heaters are installed.

Examples of possible instrumented tower configurations are shown in Fig. 17.5. The schematic in Fig. 17.5a presents a configuration that was used for the evaluation of eddy diffusivities of momentum and heat

$$K_M = -\frac{\overline{u'w'}}{\left(\frac{\partial U}{\partial z}\right)} \quad (\text{momentum}), \quad (17.10)$$

$$K_H = -\frac{\overline{w'\theta'}}{\left(\frac{d\theta}{dz}\right)} \quad (\text{heat}), \quad (17.11)$$

when the wind direction was constant with height. Here the fluxes of momentum ( $\overline{u'w'}$ ) and heat ( $\overline{w'\theta'}$ ) measured by the lower sonic (height 4.5 m) are used together with gradients of the mean wind ( $\partial U/\partial z$ ) and temperature ( $d\theta/dz$ ) measurements of two cup anemometers and two thermistors placed below and above the sonic (heights  $\approx 2$  m and  $\approx 7$  m). The fluxes are also measured by a second sonic placed at the top of the tower. In the configuration presented on Fig. 17.5b, fluxes are meas-

ured at three levels and the gradients of mean values can be calculated using the two sonics.

Hot wires are sometimes used for atmospheric velocity measurements at very high frequencies. Given their high sensitivity and fragility, constant care and protection need to be applied. For example, sand grains carried by the wind can easily break a hot wire. This type of sensors is also very susceptible to noise and has a limited measurement range in terms of flow magnitude and direction. Therefore, hot wires are mainly used under controlled laboratory conditions and only for some specific turbulence-related atmospheric boundary-layer measurements.

### 17.1.2 Temperature, Relative Humidity, and Pressure

Ordinary thermistors are usually employed for atmospheric temperature measurements. They are inexpensive, conveniently available in different varieties, adaptable, and versatile. Thermistor circuits can have reasonable output voltages – compared to the milli-



**Fig. 17.6** From the left: soil thermistors (M107), a relative humidity sensor (HMP45C), and an infrared sensor (4000.4ZL)

volt outputs of thermocouples. In field applications, proper radiation shielding is needed to limit direct solar radiation loading. To reduce the influence of solar heating further, the radiation shield can be aspirated by drawing air across the measurement junction using a high-powered fan. This, however, creates an increased power demand, which may present a problem for remote weather stations that operate solely on solar power. When fast measurements ( $> 1$  Hz) are needed, thermocouples are used. By their very nature, thermocouples are less stable and more sensitive to noise. Usually a signal gain is required for their operation, whence any noise picked up by the thermocouple will be amplified. When a fast response is needed, fine wire thermocouples are frequently used but the drawbacks stated in Sect. 17.1.1 for hot wires also apply to such fine wire thermocouples. Owing to their extremely small wire diameter, the solar loading on them is negligible, thus eliminating the need for radiation shielding.

Contact sensors used for surface measurements tend to influence the surface temperature being measured (e.g., by shading the surface from solar radiation), but maintaining a constant thermal contact with the surface is difficult. Therefore, infrared (IR) sensors are widely used for surface (skin) temperature measurements. The latter are noncontact instruments that sense emitted infrared radiation and calculate surface temperature via Stefan's law:

$$J = \varepsilon \sigma T^4, \quad (17.12)$$

where  $J$  is the measured IR radiation,  $\varepsilon$  is the surface emissivity ( $0 \leq \varepsilon \leq 1$ ),  $\sigma$  is the Stefan–Boltzmann constant ( $\sigma = 5.67 \times 10^{-8} \text{ W m}^{-2} \text{ K}^{-4}$ ), and  $T$  is the surface temperature. The emissivities for different surface types can be found in handbooks [17.2]. For greater accuracy, the sensor body temperature is used to correct

the target temperature. The IR sensor output voltage is proportional to the surface temperature.

The relative humidity (**RH**) is defined as the ratio of the actual amount of moisture in the atmosphere to the amount that the atmosphere can hold. **RH** is an important quantity in weather prediction for the estimation of precipitable water and evaluating the virtual temperature. It is also used to estimate evapotranspiration and to predict the health of plants. Water vapor is a strong greenhouse gas that acts to trap infrared radiation reflected from the Earth. Modern **RH** sensors are based on a principle that relates the changes in the capacitance of a thin polymer film when it absorbs water molecules. Such sensors yield a voltage output proportional to the relative humidity. Temperature compensation is required in computing final **RH** values, and thus a temperature sensor is needed in **RH** instruments. The accuracy of these measurements is 2–3%, depending on the absolute value of **RH** (the higher the **RH**, the lower the accuracy). As for temperature sensors, **RH** sensors also need a radiation shield. **RH** can also be obtained from wet- and dry-bulb temperature measurements. Other quantities that measure atmospheric water vapor are the absolute humidity (the mass of water vapor in a given volume of air), the mixing ratio (the ratio of the mass of water vapor contained in a sample of moist air to the mass of dry air in the sample), the specific humidity (the ratio of the mass of water vapor in a sample of moist air to the total mass of the sample), and the dew point (the temperature at which a parcel of air saturates). Figure 17.6 shows examples of temperature, **RH**, and IR sensors.

The barometric pressure (the pressure of the atmosphere) is one of the most important parameters for weather prediction, given that the movement of pressure fronts indicates the trajectory of weather fronts. A conventional barometer consists of a sealed glass tube, evacuated, and placed in an open pool of mercury; the

pressure is measured directly as the height of mercury in the tube. Modern barometers use electronic pressure transducers fitted with a pressure-sensitive diaphragm, and a sensor whose electrical (or resonant) properties change with the shape of the diaphragm. These sensors have an accuracy of  $\approx 0.3$  hPa. The barometric pressure is expressed as either the *absolute barometric pressure* (exerted by the atmosphere relative to a vacuum), or as the *corrected barometric pressure* (the absolute barometric pressure at any level adjusted to be the measurement that would result if it was done at the sea level).

### 17.1.3 Fluxes

Calculation of sensible heat fluxes using sonic anemometers measurements was described in Sect. 17.1.1. Sensible heat flux is transmitted from the surface into the air by conduction, and the breakdown of the conduction layer causes convection to transport the heat flux to higher air layers. Supplementary heat transport comes through water-vapor condensation or evaporation in the form of latent heat flux. To calculate the latent heat flux, it is necessary to measure water-vapor fluctuations in air. A commonplace instrument for this purpose is the krypton hygrometer (Fig. 17.7), which measures the absorption of ultraviolet light (two lines at 123.58 nm

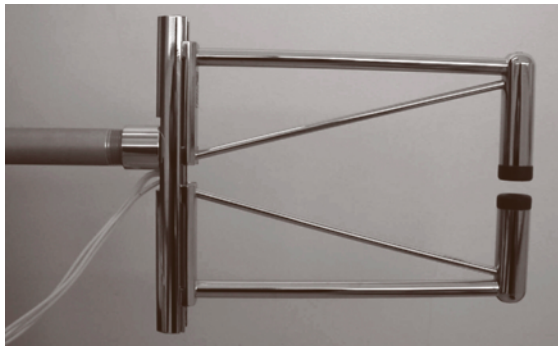


Fig. 17.7 Krypton hygrometer (KH20)

and 116.49 nm) and produces a voltage output that is a function of the instantaneous deviation of water-vapor density ( $\rho'_v$ ) from the mean. The response rate of a krypton hygrometer can be as high as 100 Hz. When used in conjunction with a sonic anemometer, or any other instrument capable of measuring fluctuations of the vertical velocity at the same rate as the hygrometer, the latent heat flux (LE) can be calculated via

$$LE = L_V \overline{w' \rho'_v}, \quad (17.13)$$

where  $L_V$  is the latent heat of vaporization, and  $\overline{w' \rho'_v}$  is the covariance between the vertical velocity and the vapor density.

The next important component of surface energy balance is the flux through the surface, usually referred to as the soil (surface) heat flux. Although our interest is flux at the air–soil surface, it is impossible to measure this directly as the flux sensor cannot be placed at the surface due to strong solar heating. Therefore, a soil heat flux plate is placed at some depth (usually 5–50 cm, depending on the soil type and amount of solar heating) to measure the thermal energy flux directly at that depth. For the surface flux calculation, it is necessary to determine the energy change in the soil layer above the soil heat flux sensor. This is achieved by placing an array of temperature sensors in the upper soil layer while the surface temperature is measured by an IR thermometer; see Fig. 17.10b for a schematic. Now the surface heat flux (SHF) can be calculated using a control-volume analysis as

$$SHF = \rho_s c_s \frac{d}{dt} \int_0^h T(z) dz + HF, \quad (17.14)$$

where  $\rho_s$  is the soil density,  $c_s$  is the soil heat capacity,  $T(z)$  are the temperatures measured in the upper soil layer,  $h$  is the depth of the soil heat flux sensor, and  $HF$  is the flux measured by the soil heat flux sensor. Modern soil heat flux sensors are equipped with a heater that performs self-calibration, during which it also determines the exact soil heat conductivity. Self-calibration

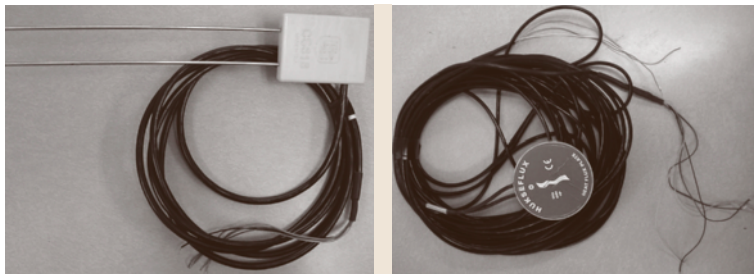


Fig. 17.8 Water content reflectometer (CS625), and soil heat flux plate (HFP01SC)



is recommended every 3–5 h. Since the soil density  $\rho_s$ , and heat capacity  $c_s$  are strongly dependent on the soil moisture content, some type of soil water content sensor, such as a *water-content reflectometer*, ought to be used simultaneously. The latter determines the volumetric water content of soils averaged over a certain depth (usually  $\approx 30$  cm) by measuring the dielectric constant of the soil. The reflectometer consists of two rods connected to a circuit board. Rods inside the soil act as antennae that transmit and receive electromagnetic signals produced by a multivibrator on the circuit board. The travel time of the signal in the probe rods depends on the dielectric permittivity of the soil, whilst the dielectric permittivity depends on the water content. Pictures of a water-content reflectometer and a soil heat flux plate are given in Fig. 17.8.

Solar radiation, its albedo, as well as the Earth's own long-wave radiation are major forcing effects for atmospheric motions and detailed measurements of these are necessary for complete energy analysis. A pyranometer measures the solar radiation  $R_S$  (short wave,  $\approx 0.3\text{--}3\ \mu\text{m}$ ), while a pyrgeometer measures far-infrared radiation  $R_{IR}$  ( $\approx > 3\ \mu\text{m}$ ). A typical setup for measuring the radiation balance consists of four sensors: a pair consisting of a pyranometer and a pyrgeometer, which face upward toward incoming solar and far-infrared radiation from the sky, and another pair, which face downward to measure the reflected solar and long-wave radiation emitted from the surface. The net radiation is given as the difference between the incoming

( $\downarrow$ ) and outgoing radiation ( $\uparrow$ ):

$$R_{\text{net}} = R_S^\downarrow + R_{IR}^\downarrow - R_S^\uparrow - R_{IR}^\uparrow. \quad (17.15)$$

As an example, five days of measurements of all four components and net radiation are given in Fig. 17.9a. These measurements were taken above a grassy area in Oklahoma City during JU2003 campaign [17.3]. Figure 17.9b shows Kipp and Zonen CNR1, Net Radiometer which has all four sensors in one assembly.

Albedo is defined as the ratio of reflected and incoming solar radiation

$$A = \frac{R_S^\uparrow}{R_S^\downarrow}. \quad (17.16)$$

Furthermore we can calculate effective sky and ground (or *skin*) temperatures as

$$T_{\text{Sky}} = \left( \frac{R_{IR}^\downarrow}{\sigma} \right)^{\frac{1}{4}}, \quad T_{\text{Ground}} = \left( \frac{R_{IR}^\uparrow}{\sigma} \right)^{\frac{1}{4}}, \quad (17.17)$$

where  $\sigma$  is Stefan–Boltzmann constant ( $5.67 \times 10^{-8} \text{ W m}^{-2} \text{ K}^{-4}$ ).

There are net radiometers that are capable of measuring directly the difference between incoming and outgoing radiation in the spectral range  $0.25\text{--}60\ \mu\text{m}$  or even  $0\text{--}100\ \mu\text{m}$ . These are cheaper but do not give information about long and short wave components (e.g.

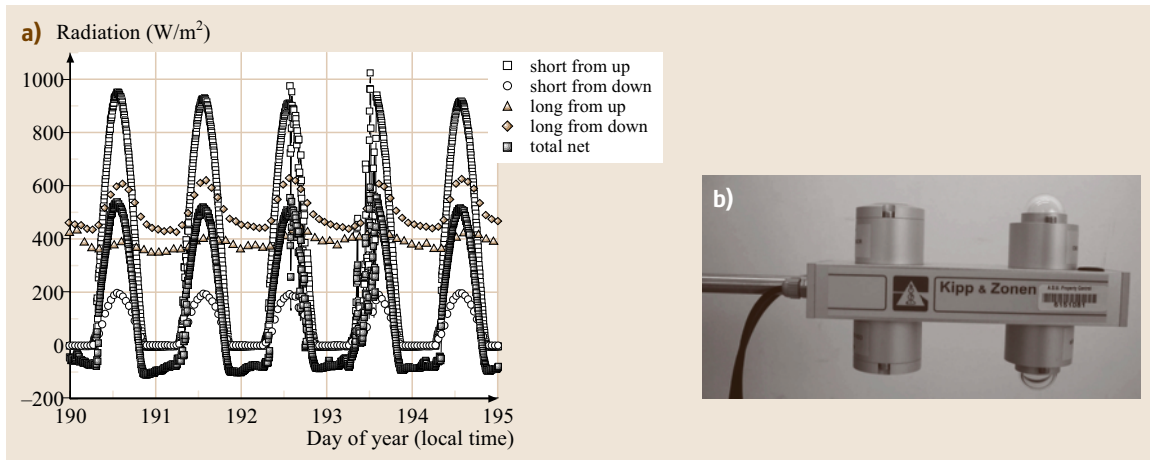


**Fig. 17.9** (a) A five-day cycle of incoming and outgoing short- ( $0.3\text{--}3\ \mu\text{m}$ ) and long-wave ( $5\text{--}50\ \mu\text{m}$ ) radiation components and total net radiation measured during JU2003. (b) Kipp and Zonen CNR1, net radiometer. Note that the pyranometers (right side of the instrument) are covered with transparent glass hemispheres to allow undisturbed passage of solar radiation. This instrument was used for the measurements presented in (a)

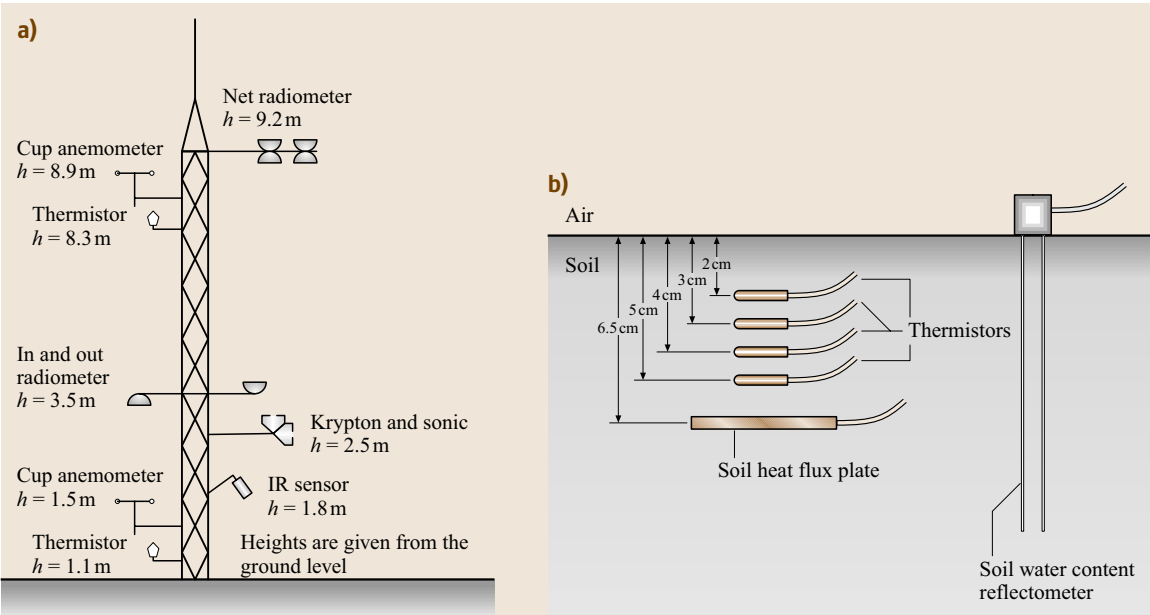


**Fig. 17.10a,b** Energy balance station used during JU2003: (a) instruments above the ground, (b) underground instruments for measuring the soil heat flux

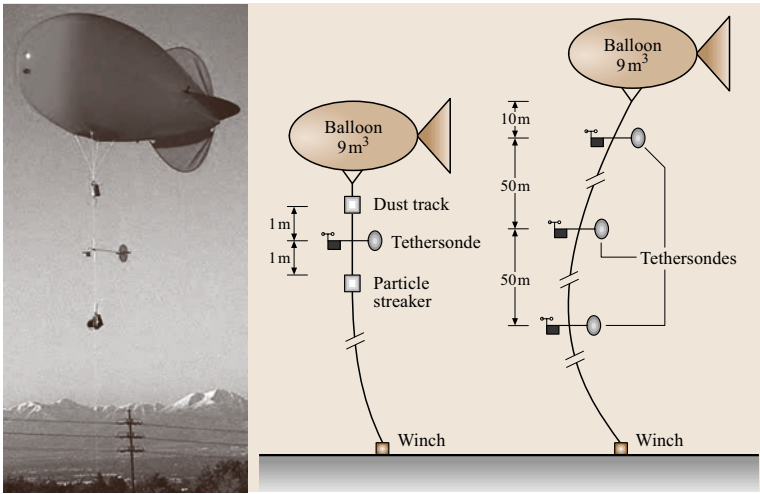


**Fig. 17.11** Tethered balloon and schematic of the setup used during the VTMX2000 campaign

calculations of albedo, surface and sky temperatures are not possible). Upon measuring these energy components, attempts can be made to close the energy budget using:

$$R_{\text{net}} = H_S + \text{LE} + \text{SHF}. \quad (17.18)$$

Note that advection is not taken into account in (17.18). It should also be borne in mind that the measured radiation

represents an average over a relatively large area, whilst sensible, latent, and soil heat flux are essentially point values (covering a relatively small area). If horizontal homogeneity cannot be assumed (e.g., due to uneven land use or roughness changes), the use of several sets of instruments spanning a larger surface area is recommended. A schematic of the energy balance setup used during the JU2003 campaign is shown in Fig. 17.10.

### 17.1.4 Vertical Profiling

Along with point measurements it is useful to acquire vertical profiles of meteorological quantities such as potential temperature, wind speed and direction, relative humidity, aerosol concentration, chemical composition, and pressure. To a certain extent, these profiles can be obtained using remote sensing techniques (Sects. 17.3 and 17.4), but at relatively coarse resolution. In high-resolution ( $\approx 1$  m) applications, tethersondes, radiosondes, and dropsondes are used for vertical profiling. A tethersonde system consists of sondes with sensors and radio transmitters, a helium balloon, an electrical winch, and a ground radio receiver. Several sondes can be used at different heights, subject to weight constraints. An electrical winch drives the tethered balloon up and down (*profile mode*) or simply keeps it at a desired height (*tower mode*). While in the profile mode, for accurate profiles, the winch speed should be commensurate with the sensor response time. A simple method of verifying that the winch speed is acceptable is to compare the consistency of two consecutive profiles (taken during balloon ascent and descent). On the other hand, by using too low of a winch speed, some small-scale phenomena may be missed, especially if the profiling height reaches several hundreds meters.

In balloon operations it should be noted that, although the winch's potentiometer setting is the same during the ascent and descent, the former velocity

will be higher than the latter, given the aiding role of the balloon lift during the ascend. This problem can be remedied by incorporating a winch controller that measures actual balloon (tether line) velocity. Figure 17.11 shows a tethered balloon that was deployed in the vertical transport and mixing (VTMX) 2000 field campaign [17.4, 5]. Three instruments can be seen attached to the tether line: a DusTrack for sampling particulate matter (the bright box closest to the balloon); a tethersonde with sensors for measuring wind speed, wind direction, temperature, relative humidity, and pressure (in the middle, with wings in the tail); and a streaker for particle collection for the purpose of chemical composition analysis (dark box below the tethersonde). Radiosondes (also known also as rawinsondes) and dropsondes essentially have the same function as the tethersondes. Radiosondes are smaller helium-filled balloons released from the ground with a single (disposable) module that collects data during ascent. Conversely, dropsondes are released from aircraft and take measurements during their descent (see Sect. 17.1).

Owing to the deflection of the balloon and instruments by horizontal mean winds, profiles taken by these profiling systems may not be strictly vertical. Modern dropsondes and radiosondes are equipped with global positioning system (GPS) devices so that their exact trajectory can be mapped. Experience suggests that the upper limit of winds for safe tethered-balloon operation is about 5 m/s.

## 17.2 Dispersion Measurements

Understanding the movement and dispersion of either gaseous or aerosolized releases in the atmosphere is an important problem in atmospheric science. The need to protect people and inform rescue and mitigation efforts in the event of catastrophic atmospheric releases is a major motivation behind this area of research. Examples of the application of dispersion-related science include responses to the Three-Mile Island nuclear accident, the Chernobyl nuclear accident, chemical attacks in the middle-eastern conflicts, and the September 11, 2001 attack on the Twin Towers in New York. Numerous field experiments and modeling efforts have focused on this problem. Some of the most frequently used measuring instruments for field experiments on atmospheric dispersion are described below.

### 17.2.1 Tracers

Two of the most commonly used tracers in atmospheric field experiments are sulfur hexafluoride ( $\text{SF}_6$ ) and perfluorocarbon (PFT) tracer gases. Both  $\text{SF}_6$  and PFT are innocuous gases and are also frequently used in the medical and industrial fields. Both are stable, colorless, and odorless. In the quantities typically used,  $\text{SF}_6$  has no known environmental or health effects. Studies in both Europe and the United States have used tracer gases since the 1960s. Many common manufacturing processes utilize  $\text{SF}_6$ . For example, the making of tennis balls, shoes, foam insulation, double-pane windows, and electrical equipment all frequently utilize  $\text{SF}_6$ . Consequently, however, it may be the case that background

levels of  $\text{SF}_6$  in urban areas may be large enough to swamp the relatively small amount of  $\text{SF}_6$  released in a dispersion experiment. Therefore, it is important to perform background testing of  $\text{SF}_6$  around the area of a proposed dispersion experiment to determine if ambient levels are too high. In these cases, which are usually in urban or industrial environments, it may be recommended to use PFTs instead of  $\text{SF}_6$ . Such deliberations are in progress, for example, at the time of writing for dispersion experiments being planned in the New York City area.

### 17.2.2 Bag Samplers

Bag samplers are one of a variety of names given to samplers containing bags which are filled by a small pump according to a schedule programmed into a microprocessor. An example is shown in Fig. 17.12. The boxes are usually battery operated and are therefore portable. Typically 12–18 sample bags are filled before the bags must be removed by hand and taken to a laboratory where a chemical analysis of the tracers is performed. The device used to perform the analysis is a gas-chromatography electron capture detector (GC-ECD).

### 17.2.3 Fast-Response Sensors

Several other types of instruments can provide analysis of tracer gas concentrations. The National Oceanic and Atmospheric Administration (NOAA)'s Field Research Division has developed a fast-response GC-ECD that produces data at about 1–2 Hz. Currently, the NOAA uses modified Sciencetech Inc. ECD devices (the TPA-4000) as the basis of their fast-response analyzers. As in the previous section, ECD stands for electron capture device and designates a type of gas chromatograph. These instruments allow atmospheric plumes of  $\text{SF}_6$  to be sampled actively in real-time with van-mounted gas analyzers. There are also several instruments that rely on some form of infrared spectroscopy. The basic idea of infrared spectroscopy is that different compounds have different vibrational states to their molecules. Vibrational states that correspond to particular frequencies of infrared light absorb infrared energy and leave an absorption deficit in the transmitted light energy. Consequently, many compounds can be identified by matching their infrared absorption patterns with those in a database. Mobile Fourier-transform infrared (FTIR) instruments operate using infrared spectroscopy principles. Recently, the *Pentagon Shield* experiments used



**Fig. 17.12** Sample boxes for the collection of  $\text{SF}_6$  gas, designed by the Lawrence Livermore National Laboratory

FTIR, bag samplers, and the TPA-4000 gas analyzers to measure  $\text{SF}_6$ . Likewise, the Thermo Electron Corporation's MIRAN SapphiRE portable infrared ambient analyzer operates on the same spectroscopy principles and has been used in several major atmospheric dispersion field experiments including the VTMX/urban dispersion experiment and the joint urban dispersion experiment in 2003 [17.4,6]. Analysis time for the MIRAN SapphiRE is 20–165 s depending on the number of wavelengths used. Typical response times are 18 s to achieve 90% of the reading. The device weighs about 10 kg and can operate on batteries for about four hours.

### 17.2.4 Recent Major Field Experiments

There has been a high level of interest and participation in field experiments in the last four years. In particular, the Department of Energy (DOE) VTMX/urban dispersion experiment and the joint urban dispersion experiment were two of the largest field experiments conducted with a focus on urban dispersion.

The VTMX/urban dispersion experiment was conducted in Salt Lake City in the fall of 2000. It was actually a combination of two experimental campaigns. The purpose behind the combination was to extend the reach and density of the relevant data for each experiment. The VTMX experiment was designed to improve the understanding of vertical transport and mixing pro-



cesses in urban meteorological basins – particularly at night. Some of the science issues motivating the study are mentioned briefly here [17.4]. One science question concerned cold pools and the nature of the interaction between cold pools, drainage flows, and larger-scale synoptic forcing. Of particular interest were the patterns of pollutant dispersal throughout the valley. How do nocturnal flow phenomena at various scales in an urban valley affect the patterns and dispersion of tracers? How can improvement in the fundamental understanding of mixing processes lead to better mesoscale, large-eddy, and direct numerical modeling? A wide variety of instruments, using both in situ and remote sensing, were deployed as part of the campaign. The distribution of the instruments was an important characteristic of the VTMX campaign – there was a basin-wide distribution and corresponding basin-wide science focus. Remote sensing instruments deployed were radar wind profilers [some with radio acoustic sounding systems (RASS)], sodars, backscatter lidars, several coherent Doppler lidars, and a Raman water-vapor lidar. Tethered balloons and rawinsondes provided vertical profiles of wind velocity, temperature, and humidity. Three-dimensional sonics were also deployed, and a number of surface data stations already existed as a part of the MesoWest network. For the tracer releases, Brookhaven National Laboratory provided perfluorocarbon tracers (PFTs). Some releases were downtown, while other locations were near the slopes or mountain valley openings. An array of instruments to measure both particles in the air and CO were also deployed to study pollution accumulation within the valley. The NOAA/ATDD (atmospheric turbulence and diffusion division) LongEZ instrumented aircraft measured the horizontal structure of wind, temperature, and turbulence on several nights. A microbarograph array was operated to capture perturbations in the surface pressure potentially associated with gravity waves.

The urban dispersion campaign associated with VTMX was specifically designed to provide data to improve and test atmospheric dispersion models. Central to the focus and design of the experiment was a dense array of instruments (both to measure tracers and meteorolog-

ical variables) deployed close to a downtown release location. The type of tracer used was SF<sub>6</sub> (some PFTs were released downtown by VTMX researchers), and all the various gas measurement devices examined above were deployed: FTIR, GC-ERD, bag samplers, and Miran gas analyzers. A total of 201 samplers were used: 56 PFT samplers, 105 SF<sub>6</sub> samplers, and 40 SF<sub>6</sub>/PFT samplers [17.6]. In addition to a dense array of instruments in several blocks around the release site, samplers were located around arcs at two, four, and six kilometers from the release site. The intention of the deployments was to provide a dataset of concentrations that could track a short-duration release around individual buildings, through city blocks, and continuing through the urban area out to tens of kilometers from the release site. A hierarchy of dispersion models could be tested with this data, from LES (large eddy simulation) models close to the release source point, to simpler models using urban roughness parameterizations. There were 10 intensive observation periods (IOPs) with nocturnal releases.

In July 2003, the Department of Defense Defense Threat Reduction Agency (DTRA) and the US Department of Homeland Security (DHS) conducted a joint study in Oklahoma City, known as the Joint Urban 2003 (JU2003). The list of instruments deployed was similar to that of the VTMX/urban dispersion experiment with some additional notes. To the knowledge of the authors, it was the first time that two, matched, coherent Doppler lidars were deployed in a coordinated fashion in a major experiment. The lidar teams experimented with several strategies to explore and optimize the combined gathering of data for regions between the two lidars. For example, data were specifically taken for the purpose of 4DVAR (four-dimensional variational data assimilation) analysis. Intersecting RHI scans between the two lidars provided a unique opportunity to explore the concept of *virtual towers*. A helicopter-based remote SF<sub>6</sub> sensor was also deployed, providing images of SF<sub>6</sub> dispersal. Indoor tracer measurements were also conducted to measure the transport of SF<sub>6</sub> through the building envelope. The first six IOPs occurred during daylight hours, in contrast to the VTMX/urban dispersion experiment outlined above. The final four IOPs took place at night.

## 17.3 Remote Sensing

### 17.3.1 Lidar

A variety of types of lidar are currently used to probe the atmosphere. In the following, an introduction to the prin-

ciples of coherent Doppler, backscatter, and differential absorption lidar (DIAL) is provided.

The general principle of coherent Doppler lidar is that pulses of laser light of a given frequency are sent

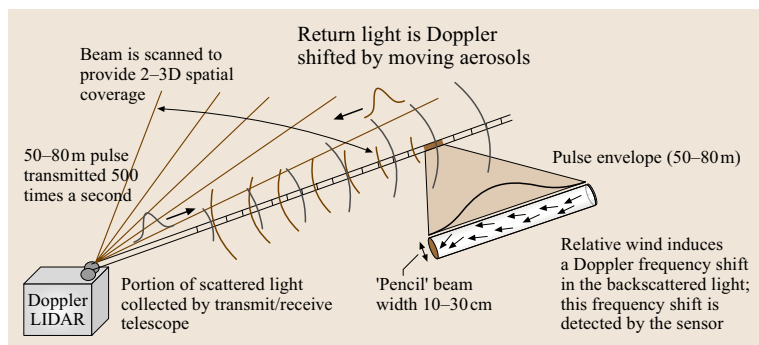


**Fig. 17.13** Principle of operation of coherent Doppler lidar (courtesy of Lockheed Martin Coherent Technologies)

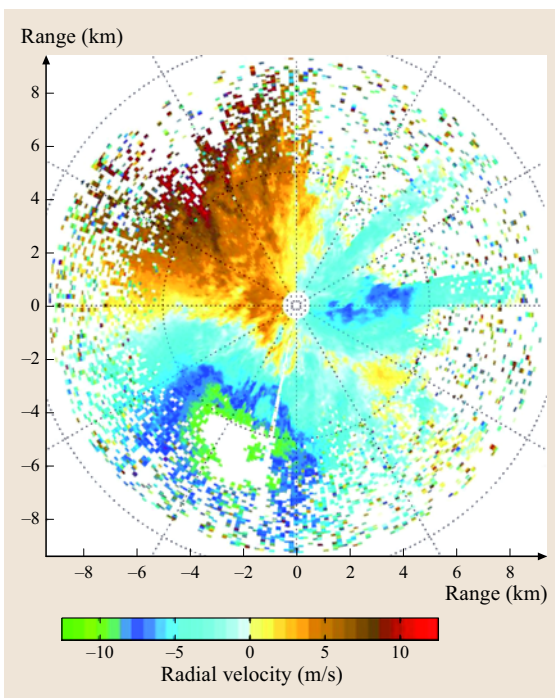


**Fig. 17.14** Example of radial velocity fields taken from the VTMX field experiment in October 2000 in Salt Lake City. A full 360° PPI is shown

out into the atmosphere and returns are collected. Ambient aerosols scatter the laser light and a fraction of the light returns to the receiver/emitter. After a single pulse is emitted, the lidar waits for returns for a time corresponding to the outer length of its range. Modern coherent Doppler lidar may have high pulse-repetition frequencies (PRF). For example, Arizona State University's lidar emits 500 pulses per second. Because the returns are collected in discrete periods or *bins*, a distance can be associated with each time *bin* according

to the distance that light can travel in the time measured. Therefore, the data is broken into range gates. For example, a modern coherent Doppler lidar may have 100 range gates, each 65 m long, for a total range of 6.5 km.

Doppler lidars have recently become available in commercial form, for example, Lockheed Martin Coherent Technologies' *WindTracer* (<http://www.lockheedmartin.com/coherent>). The principles of operation of this type of lidar are illustrated in Fig. 17.13. (The physical details described are for Arizona State University's Doppler lidar built by Lockheed Martin Coherent Technologies Inc.) Five hundred pulses of infrared laser light are sent into the atmosphere each second. The laser pulses are shaped like rods typically 50–80 m long and 10–30 cm in diameter, depending on the distance from the lidar. In addition to the range resolution based on discretely measuring the time of return for backscattered light, aerosols along the path of the beam impart a Doppler frequency shift proportional to velocity of the aerosols in the direction parallel to the laser beam. Therefore, both the range and radial velocity are measured. By scanning the laser beam, the two- and three-dimensional structure of the radial velocities and aerosol levels can be obtained using the RHI and PPI modes described in Sect. 17.1.

A typical example of a PPI radial velocity field is given in Fig. 17.14. The location of the lidar is at the center of the graphic. Blue colors represent velocities moving towards the lidar and orange–red colors indicate velocities away from the lidar. The lidar deployment was part of the DOE VTMX and urban dispersion experiment in October 2000 in Salt Lake City. Note that on the right side of the plot a drainage flow (darker blue) coming down from the surrounding Wasatch mountain range can be seen. This was a frequent occurrence in the evening hours during the VTMX experiment. The blue patterns to the left and down from the center and the brown/orange

to the left and up from the center are evidence of a larger scale up the valley flow (from south to north).

Examples of RHI plots are shown in Figs. 17.15, 16. Both plots are from the JU2003 deployment of the Arizona State University lidar in Oklahoma City. These scans used the same look direction at different times and were chosen to show examples of the quiescent boundary layer (Fig. 17.15) and more-active conditions (Fig. 17.16).

While the Doppler frequencies measured with a coherent Doppler lidar are known with reasonably well-defined accuracy, estimating concentrations of aerosols from the strength of the return signal is fraught with difficulties. An important distinction should be made between the power signal received back at the lidar after a pulse is transmitted and the concentrations of aerosols. One can view the lidar equation (17.19) in order to understand this problem more carefully. This version of the equation is valid for single elastic backscatter of the laser light off aerosols and is appropriate for the coherent Doppler lidar.

$$P(r) = \frac{C}{r^2} \beta(r) e^{-2 \int_0^r k(r') dr'}, \quad (17.19)$$

where  $r$  is the distance of a range gate from the lidar,  $P(r)$  is the power received from the range  $r$ ,  $\beta(r)$  is the volumetric backscatter coefficient of the atmosphere at range  $r$ ,  $k(r)$  is the corresponding extinction coefficient at range  $r$ , and  $C$  is the lidar constant (a function of the physical characteristics of the device).

Note that the power  $P(r)$  is a function of both the extinction coefficient (i. e., the integrated degradation in the signal caused by absorption of light along the beam path) and the backscatter at the location  $r$ . The backscatter is dependent on the concentration of the aerosols; however, it is also dependent on the size distribution, shape, and composition of the aerosols. Therefore, there are significant difficulties associated with inversion of the lidar equation in order to obtain concentration. Furthermore, simplifications such as the use of Mie theory, which assumes spherically shaped particles, to relate backscatter to concentration may be poor approximations. Notice that in the lidar equation (17.19), both the backscatter and extinction are unknown. Therefore, to relate the power  $P(r)$  to the backscatter requires some additional information or assumptions to be supplied. Some researchers have proposed various relationships between backscatter and extinction. Even if backscatter could be obtained, there are significant challenges in relating backscatter to concentration. Formally, one must know the composition, shape, and size distribution of

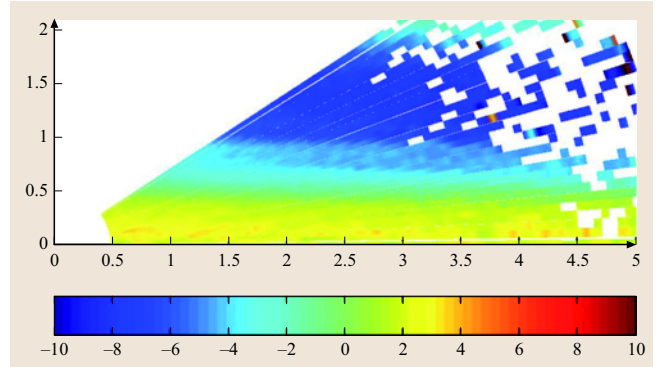


**Fig. 17.15** RHI plot of winds in Oklahoma City during the JU2003 Experiment, 7/15/03 at 10:40 UTC. Note the rather quiescent boundary layer and compare with Fig. 17.16 below. Range away from the lidar is in kilometers directly below the plot, and the color bar shows how color relates to radial velocities

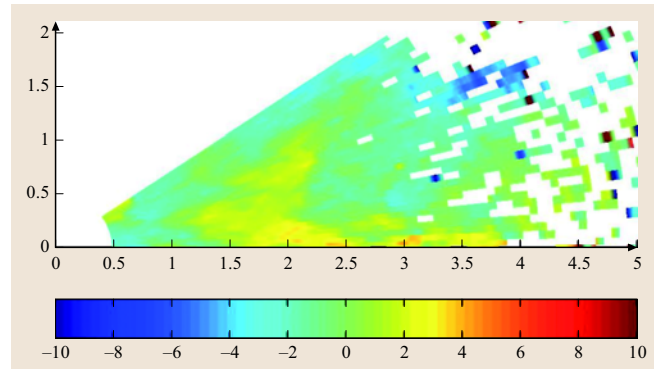


**Fig. 17.16** RHI plot of winds in Oklahoma City during the JU2003 experiment, 7/14/03 at 20:20 UTC. Note the more-active boundary layer compared with Fig. 17.15. Range away from the lidar is in kilometers directly below the plot, and the color bar shows how color relates to radial velocities

aerosols at all the sampling locations. It may be possible to measure the characteristics of the aerosols at one or more points with in situ instrumentation, but the question of the validity of assuming the homogeneity of these characteristics over the lidar sampling area remains.

Backscatter lidars receive range-gated light returns similar to coherent Doppler lidar except a frequency shift cannot be measured. Backscatter lidars are relatively simple, typically monochromatic with only one transmitter and receiver channels. The same issues relating to difficulties inverting the equation describing the power returned to the receiver apply. It is usually implied that a backscatter lidar sends out a given frequency

pulse and receives back that same frequency, i. e., light is elastically backscattered without a frequency shift (as opposed to Raman lidar).

Differential absorption lidar (DIAL) measurements are made with at least two different wavelengths of laser light. The most typical use of DIALs is to monitor trace gases. One wavelength is chosen so that it is absorbed maximally by the given trace gas, and the other is chosen so that it is not absorbed. The ratio of the power returned between the two types of pulses (that absorbed and not) is related to the amount of the target trace gas along the path. DIAL is also sometimes used to obtain atmospheric temperature. In this case, a target gas that does not vary significantly across the atmosphere is chosen, and the relational dependence between absorption and density, pressure, and temperature is utilized. The DIAL technique can be very sensitive and can be quite useful for monitoring pollution gases in urban areas. DIALs that detect ozone gas have been used to map the severity and extent of ozone events in major cities. It is particularly useful for this application to mount the DIAL on an aircraft.

### 17.3.2 Ceilometers

Laser ceilometers are pulsed, backscatter laser systems without scanning capability and without the ability to detect the Doppler shift from the returns. The returns are range-gated so that the distance (or ceiling) of the strong backscatter signal from clouds can be measured. Owing to the lack of a need for scanning motors



**Fig. 17.17** The ceilometer deployed during the DOE VTMX urban dispersion experiment in Salt Lake City 2000. This small, lightweight device was provided by Vaisala, and is the CT25K model

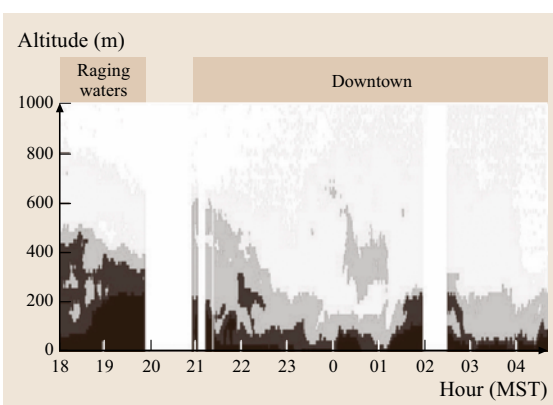


**Fig. 17.18** The output of the ceilometer (backscatter signal) showing aerosol layers during DOE VTMX/Urban Dispersion Experiment in Salt Lake City 2000

and simpler signal-processing requirements, ceilometers are quite compact compared to coherent Doppler lidars (Fig. 17.17).

The data produced by ceilometers is  $P(r)$ , similar to the coherent Doppler lidar described above. Subject to the same caveats noted in the previous section, the output is frequently given in terms of aerosol backscatter. In this case, assumptions with regard to extinction are implied. The strength of ceilometers is their robust ability to accurately determine (within tens of meters typically) ceiling heights of cloud layers. Off-the-shelf ceilometers that are easy to operate and need not be attended for long periods can be purchased. In recent years, ceilometers have been used in larger experiments to locate layers of aerosols in the boundary layer and to help determine boundary layer heights. For example, the authors have experience with deployment of a Vaisala CT25k during the DOE VTMX/urban dispersion experiment in Salt Lake City [17.7]. Usual vertical resolutions are 10–30 m. During the VTMX experiment, the ceilometer showed evidence of nocturnal layers and occasional wavy behavior within these layers (Fig. 17.18).

### 17.3.3 Sodar

The general principle of sound detection and ranging (sodar) is that acoustic energy scatters back off temperature variations in the atmosphere. Acoustic pulses are sent out into the atmosphere, usually at frequencies of 1000–4500 Hz. For reference, the human ear can respond to a frequency range of 20–20 000 Hz. Consequently, sodar signals are frequently audible. The corresponding wavelengths of sodar frequency ranges



are in the tens of centimeters. Since sound waves interact with inhomogeneities in the atmosphere similar to their own size, temperature variations in the range of 10–30 cm typically cause backscatter to occur. The backscatter is range-gated in the same manner as for coherent Doppler lidar, i.e., the time of return for the backscatter signal is translated into distance using a speed constant (the speed of sound for sodar vis-à-vis the speed of light for lidar). The Doppler shift of the returning signal is analyzed to provide the radial velocity of the sampling volume. Three directions or beams are required to recover the full velocity vector using simple geometrical arguments. This can be accomplished with three, physically separate, sound drivers, or with a phased array of many speakers (some arrays with more than 100). By precisely controlling the phase of the speakers, electronic steering can be accomplished.

Two main types of sodars exist: monostatic and bistatic. Monostatic sodars have the receiver and transmitter collocated, while in bistatic sodars there is a separation between the receiver and transmitter. Most commercial systems use the monostatic approach because of efficiencies of cost and construction associated with collocated receivers and transmitters. Sound will backscatter off of both mechanical and thermal inhomogeneities caused by atmospheric turbulence. However, only the thermal inhomogeneities backscatter at 180°. Therefore monostatic systems rely on backscatter off thermal variations in the atmosphere. Bistatic sodars can use backscatter off both mechanical and thermal variations because the separation between the receiver and transmitter implies that smaller backscatter angles will still reach the receiver. In principle, this should result in more-robust returns, but the aforementioned efficiency of monostatic systems appears to dominate sodar design decisions.

Another important difference between monostatic and bistatic sodars is in the sampling volume. Monostatic devices have all receivers and transmitters in one location and point towards different volumes. Obviously, some degree of horizontal homogeneity of winds is implied when using monostatic sodars. This is due to the fact that different observation directions for sampling a (horizontally homogeneous) region of winds must be used in order to obtain different components of the velocity. A full velocity vector requires three observation directions. Bistatic sodars may have one, upward-looking, collocated receiver/transmitter, and two additional transmitters angled to overlap the

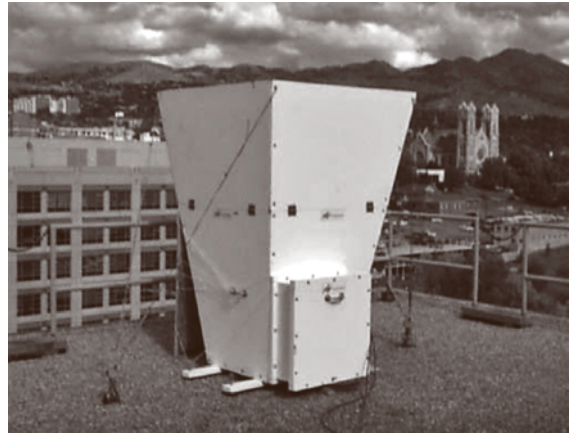


**Fig. 17.19** Sodar deployed by the U.S. Army Dugway Proving Grounds during the DOE VTMX/Urban Dispersion Experiment (Courtesy C. Biloft)

central beam. Consequently, the assumption of homogeneity need only apply to the overlapping volume (three intersecting cones). Monostatic Doppler sodars usually perform better than phased-array systems.

Sodars typically have ranges from the tens of meters up to 1000 m with vertical resolutions of 10–50 m depending on the configuration and manufacturer. Mini-sodars often have a maximum vertical range of a few hundred meters. General characteristics of sodars that are important to keep in mind when comparing with other measurement devices are:

1. the relative low cost to operate and purchase
2. known accuracies and much previous experience
3. good near the ground, but somewhat limited performance in upper air measurements
4. sound contamination must be considered in choosing a location
5. signal in audible range, so people around the deployment may be annoyed by operating the sodar, and
6. ground clutter can cause difficulties by biasing the recovered wind toward zero, i.e., nearby trees or buildings may cause problems.

In the DOE VTMX/urban dispersion experiment (Fig. 17.19), for example, it was found that initially a sodar on a high-rise building in downtown Salt Lake City (surrounded by other buildings) was experiencing echoes from nearby buildings. The solution was to reorient the noisier side of the sodar away from neighboring high-rise buildings.

### 17.3.4 Radar Profilers

Radio detection and ranging (radar) profilers are similar to sodars in principle, except that they use radio rather than sound waves. Three to five near-vertical observation directions are used to obtain radial velocities using the Doppler shift of backscattered radio waves. The frequencies of radar profilers have been adjusted compared to other radars to have enhanced interaction with refractive-index regularities caused by turbulence. Refractive-index fluctuations are advected by the wind, and because they can be detected by the radar, an estimate of the wind moving along the radio beam can be obtained. Similar to Doppler lidar and sodar, different observation directions and the assumption of wind homogeneity over a measurement area can be used to produce velocity vectors with simple geometri-



**Fig. 17.20** The 915 MHz phased-array radar and Doppler sodar (right) deployed by NOAA's Air Resources Laboratory in Idaho Falls. These instruments were deployed as part of the DOE VTMX/urban dispersion experiment in Salt Lake City 2000

cal arguments. Figure 17.20 shows an NOAA 915 MHz radar profiler deployed in Salt Lake City for the DOE VTMX/urban dispersion experiment in 2000.

Several characteristics of radar profilers should be kept in mind relative to other types of profilers. Radar profilers typically have much higher vertical ranges than sodars. The NOAA 915 MHz radar in Fig. 17.20, for example, has a range from 150–4000 m and vertical resolutions in the range of 10–50 m. Like sodar, radar profilers are commercially available – with boundary or lower-atmospheric ranges up to 3–4 km – to tropospheric profilers that can measure up to 16 km vertically. Extra vertical range is usually achieved at the expense of vertical resolution. Secondly, the radio energy from radar is not as focused as the energy from a lidar. This allows increased backscatter from the sides of a much broader observation direction. Consequently, ground clutter can prevent useful data from being obtained near the ground. Radar profilers are typically deployed in tandem with sodars (Fig. 17.21). The latter performs well near the ground, whereas radar profilers can provide high vertical range. Third, it should be recognized that with higher vertical range comes much more extensive assumptions of homogeneity of winds associated with the reconstruction of radial velocities from three different observation directions into velocity vectors. At 10 km above the Earth's surface, obtaining wind vectors may imply an assumption of wind homogeneity on the 3 km scale. Lastly, radar technology is mature and these devices typically operate well in an unattended mode.

### 17.3.5 RASS

Early versions of radio acoustic sounding systems (RASS) were tested in the 1960s. The result of a RASS is the virtual temperature. Because there is a known relationship between the speed of sound and the virtual



**Fig. 17.21** Example of co-located remote sensing instruments during the joint urban dispersion experiment 2003 in Oklahoma City (from left: sodar, ceilometer, radar). (Photo courtesy of Lawrence Livermore National Laboratory)

temperature in the atmosphere Sect. 17.3), measurements of the speed of sound at various levels in the atmosphere can be translated into virtual temperatures at each level. Collocated acoustic and radar profilers, as seen in Figs. 17.20, 21, can be used to obtain the speed of sound by backscattering radio energy off vertically propagating sound waves. Sound waves moving through the atmosphere change the refractive dielectric constant and may backscatter radio energy of an appropriate wavelength. By varying the acoustic frequency of a sodar, one can find the optimal frequency so that the radio waves from a given radar will backscatter strongly off the sodar's acoustic waves.

Time-of-arrival and Doppler shift information provide vertical range and speed of sound measurements. Early in the development of RASS technology, it was not easy to use the radar in a mode to acquire both profiles of radial velocities (i.e., as a radar profiler) and to track the vertical propagation of an acoustic wave. With more development, this has become possible and consequently RASS devices have access to both radial velocities and the acoustic propagation speeds at the same time. As a result, radial velocities can be used to improve the accuracy of the speed of sound measurements. The measured Doppler shift in a RASS is

a projection onto the observation direction of a vector sum of the acoustic wave velocity vector and the wind vector. If the radial wind velocity is known, it can be subtracted off and a more-accurate virtual temperature can be obtained.

Some of the limitations of RASS are related to the advection of acoustic waves by the background wind and to distortion by turbulence. Therefore, the acoustic wave, which is intended to be located directly above the radar, can be off center due the background wind, and consequently, the vertical range may be comprised. However, beam-steering techniques that allow maximum ranges of up to 20 km to be obtained have been developed [17.8]. Depending on the frequency of the radar used, the appropriate corresponding acoustic signal may be attenuated in different ways. For example, ultrahigh frequency (UHF) RASS is more strongly limited vertically than very-high frequency (VHF) RASS. Another characteristic of RASS is that they are frequently very loud and need to be placed away from people. Since the output is virtual temperature, one would require additional information about moisture to obtain standard temperature. For this purpose, one might envision a collocated water-vapor DIAL lidar and a RASS.

## 17.4 Satellite Measurements

Technological breakthroughs in the 1990s have led to extraordinary advances of remote sensing capabilities for the 21st century and hence to the emergence of a new topical area known as satellite meteorology, which deals with the study of the Earth's atmosphere and oceans using data obtained from remote sensing devices onboard satellites. The enhanced remote probing capabilities are utilized by dozens of satellites continuously collecting data from multiple vantage points, allowing scientists from different continents to collect and share data. There are two main types of meteorological (weather) satellites, defined by their orbital configurations that essentially determine the surveillance characteristics: geostationary and polar-orbiting satellites. The former move in prograde orbits [GEO (Geostationary Earth Orbit);  $\approx 35\,000$  km high] above the equator whereas the latter circle the Earth from pole to pole twice a day. Some examples of the geostationary satellites are the US geostationary operational environmental satellites (GOES) (two in service, GOES-12 and GOES-10, looking at the east and west coasts), the European METEOSAT, and the Japanese Geostationary

Meteorological Satellite (GMS). Weather forecasting and presentations are based on these satellites. Operationally two polar-orbiting satellites are employed, one satellite passing south to north (ascending; e.g., the US Aqua satellite) and the other vice versa (descending; e.g. the US Terra satellite). These can be placed in sun-synchronous orbits, which place the ascending node at a constant solar time, permitting images to be taken at a given location received at the same time each day. These satellites are used for special purposes, such as monitoring of snow and ice sheets, but because of the viewing geometry their images need to be assembled as mosaics. Also of utility are the polar operational environmental satellites (POES) on low-Earth orbits (LEO  $\approx 880$  km) that travel from pole to pole on a shorter time scale (orbital time  $\approx 1$  h 42 min). These satellites collect data in a swathe as the Earth rotates beneath them, and yield high-resolution images and atmospheric profiles.

Flown on board these satellites are radiometers that measure either reflected or emitted electromagnetic radiation by the Earth's surface or atmospheric constituents in a series of discrete spectral bands. The measurements

are transmitted back to the Earth, usually in the form of an image. Since each type of surface material on the Earth and each type of particle in the atmosphere has its own unique spectral signatures, the data can provide valuable information about the target. Two types of radiometers are used: imagers (which provide information on visible light from the sun reflected back to space by the Earth's surface or clouds), and sounders (which measure the amount of radiation emitted). Most commonly used sensors belong to the categories of visible, infrared (IR), water-vapor, and microwave sensors.

Visible sensors operate in a spectral range of  $0.55\text{--}0.99\text{ }\mu\text{m}$ , and the amount of shortwave radiation detected therein is a function of the reflectivity of the target; for example, cloud tops and the Earth's surface. The images so obtained are similar to black-and-white photographs of the Earth. The brightest and whitest elements of these images indicate the most-reflective surfaces, such as thick clouds or fresh snow cover, whereas the darkest parts indicate the least reflective surfaces, such as the ocean surface (nearly black). Differences in the shading of clouds usually relate to cloud thickness. Land surfaces tend to appear gray. Some of the interesting features that may be visible in visual images include the sun glint or glitter (a large bright region due to the reflection of the sun off a large water surface), shadows (due to clouds when the sun angle is low or overshooting tops in tall thunderstorm clouds), terminators (shadow from the dark side of the earth), terrain features (lakes, rivers, mountains, snow cover or differences in reflectivity due to large forests), and snow cover (depending on the age and thickness of snow and ice).

IR sensors measure radiation at wavelengths of  $10.3\text{--}12.6\text{ }\mu\text{m}$ , wherein cold objects appear white and hot surfaces black. For example, interplanetary space beyond the limb of the planetary disk appears white on IR images because of the extremely cold temperatures of space. This feature can be used to distinguish IR imagery from visible images. The IR sensor band is within a reasonably transparent *window* region of the atmosphere, and in cloud-free regions the long-wave radiation from the radiating Earth's surface can be detected by IR sensors both during the day and night. The Stefan-Boltzmann law determines the amount of IR radiation and its spectral quality, and thus the absolute temperature of the radiating objects (e.g., land, water, and clouds) can be measured remotely using IR sensors. Such imagery can also be used to distinguish low clouds (which are relatively warm and appear gray, as in the case of fog) from high clouds. Thick cold clouds, like the tops of thunderstorms, appear bright white. Methods

have been developed to estimate the physical thickness of the clouds and the temperature and altitude of the cloud base [17.9] using satellite data and other information sources. A milky appearance over an otherwise cloud-free region may indicate an exceptionally cold air mass. Surface features can be detected in IR imagery by subtle shading contrasts resulting from differences in the surface temperatures. For example, cloud-free ocean regions appear more uniform because of more-uniform sea surface temperatures, whereas large differences in surface temperature over continents produce images with dark regions over hot deserts and lighter regions over mountainous terrain.

Water-vapor imagery is a valuable tool for weather analysis and forecasting, because it represents flow patterns of the upper troposphere. Water vapor is transparent to visible and IR wavelengths and thus are invisible to IR satellite imagery, but it is a very efficient absorber and emitter in the  $6.5\text{--}6.9\text{ }\mu\text{m}$  band (which is technically an IR band, but operating at a different band from the usual IR sensors). Thus radiometers sensitive to this band can be used to detect water vapor in the atmosphere (typically displaying water-vapor concentrations of  $5\text{--}9\text{ km}$ ). Black indicates low amounts of water vapor and milky white indicates high concentrations. Bright white regions correspond to cirrus clouds. In the middle latitude regions, zones with strong contrast in the amount of water vapor often indicate the presence of a jet stream.

Some satellites have a scanning microwave radiometer that senses the microwave (far infrared) radiation emitted by the Earth with wavelengths in the vicinity of  $1.5\text{ cm}$ . In essence, a microwave detector can penetrate clouds and distinguish between ground and ice or snow surfaces. However, these sensors offers poor spatial resolution.

Spectral data about a target across a range of energy levels can be obtained using multispectral remote sensors, which is comprised of an array of sensors, each tuned to a particular channel or band of wavelengths. For example, weather satellite sensors are designed to probe the visible, near-infrared, and thermal infrared radiation from various surface materials and atmospheric components. The radiometers on land-use satellites such as Landsat and Spot are engineered to provide multispectral data that aids in measuring the spectral differences between various surface materials. Different land surface types such as concrete, asphalt, crops, meadow, forest, water, and desert all exhibit unique spectral signatures. An example of images taken from the advanced space-borne thermal emission and reflection radiome-



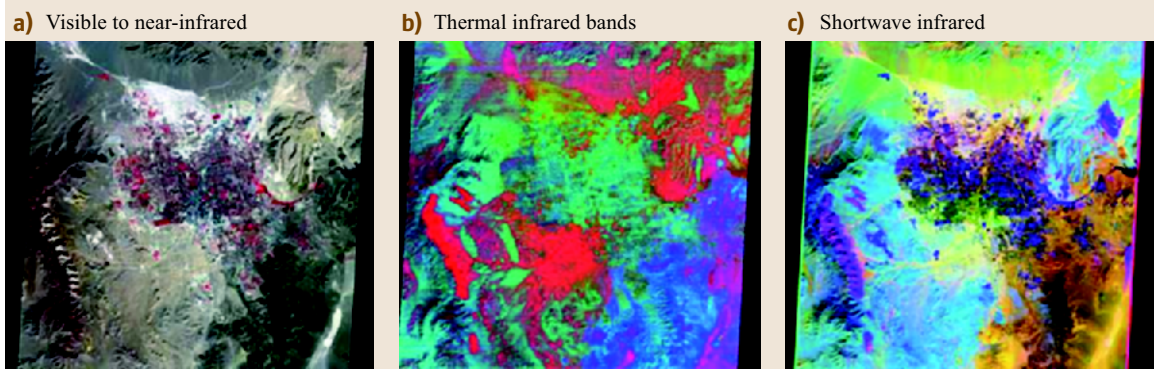


**Fig. 17.22a–c** Images obtained by ASTER at different wavelength bands (Courtesy of Will Stefanov, ASU). (a) Visible to near-infrared, (b) thermal infrared bands, (c) shortwave infrared

ter (ASTER) instrument onboard the Terra satellite in the visible to near-infrared (15 m/pixel resolution), short-wave infrared (30 m/pixel), and thermal infrared (90 m/pixel) is shown in Fig. 17.22. Using the visible to near-infrared band, it is possible to obtain information on major land-cover classes, vegetation health, soil properties, and soil contamination. Thermal infrared bands are used for evaluating surface energy balances, regional climate models, anthropogenic heat sources, and heat island development. Shortwave infrared bands are used for studies on urban surface materials, rooftop materials, energy use, fugitive dust production, and metal contamination.

The geosynchronous imaging Fourier-transform spectrometer (GIFTS) with  $\approx 1600$  channels in the thermal infrared spectral region, which is slated to be launched before 2010, is expected to provide new capabilities for measuring turbulent fluxes at the land surface.

Satellite-borne instruments are an invaluable tool for monitoring numerous environmental phenomena, such as fires, stack plumes, and air pollution. Wind vectors from satellite images are calculated using two techniques: tracking moisture gradients using ( $6.7\ \mu\text{m}$ ) water-vapor images, and detecting a cloud and tracking its motion through a sequence of images; the latter method is commonly applied to IR-window and visible images. Observations at a wavelength of approximately  $4\ \mu\text{m}$  are used to detect fog at night, discriminate between water clouds, ice clouds, and snow, detect fires and volcanic eruptions, and to meas-

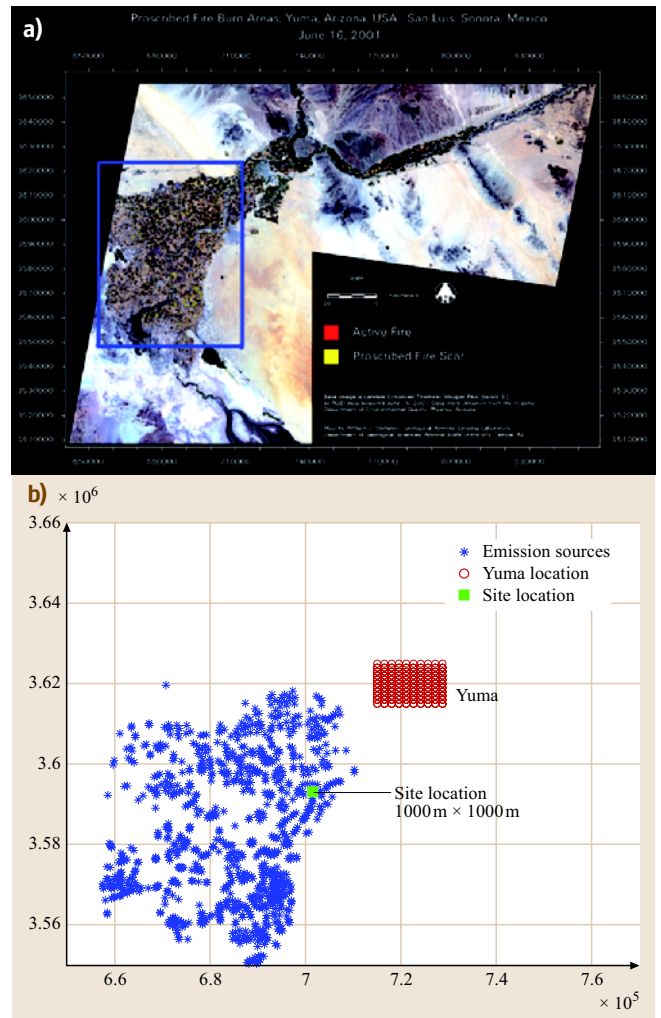


**Fig. 17.23** (a) Fire scars in the Yuma/San Luis area, obtained by ETM+, and (b) the processed image of the boxed area using a pattern recognition technique

ure the temperature of the ocean during the night. The fires and smoldering fire scars appear as *hot spots*. This is evident from Fig. 17.23a, which was constructed using the reflectance in the visible through shortwave infrared portions of the spectrum of images acquired by the enhanced thematic mapper plus (ETM+) instrument orbiting onboard the Landsat 7 satellite (30 m/pixel ground resolution). In this case, the locations of agricultural burns in the Yuma-San

Luis airshed surrounding the US–Mexico border were monitored to evaluate the plume pathways using dispersion models. Figure 17.23b shows extracted fire scars using a special algorithm. Once active fires and smoldering regions can be identified, respective emission factors can be used to model the dispersion of contaminants from agricultural fires. Such contaminants are believed to have health impacts on US–Mexico border communities.

## References

- 17.1 Campbell Scientific Inc.: *CSAT3 Three Dimensional Sonic Anemometer, Instruction Manual* (Campbell, NorthLogan 1998)
- 17.2 T.R. Oke: *Boundary Layer Climates*, 2nd edn. (Methuen, New York 1987)
- 17.3 M. Princevac, R. Calhoun, D. Zajic, J.E. Holeman, R. Heap, H.J.S. Fernando: Arizona State University's contribution to the Joint Urban 2003 experiment: an overview. In: *Proc. Tenth Asian Congress of Fluid Mechanics* (University of Paradeniya, Paradeniya 2004)
- 17.4 J.C. Doran, J.D. Fast, J. Horel: The VTMX 2000 campaign, *Bull. Am. Meteorol. Soc.* **83**(4), 537–554 (2002)
- 17.5 P. Monti, H.J.S. Fernando, M. Princevac, W.C. Chan, T.A. Kowalewski, E.R. Pardyjak: Observations of flow and turbulence in the nocturnal boundary layer over a slope, *J. Atmos. Sci.* **59**(17), 2513–2534 (2002)
- 17.6 K.J. Allwine, J.H. Shinn, G.E. Streit, K.L. Clawson, M. Brown: Overview of URBAN 2000; a multiscale field study of dispersion through an urban environment, *Bull. Am. Meteorol. Soc.* **83**(4), 521–536 (2002)
- 17.7 R. Bowen, R. Calhoun, J. Rasanen: Ceilometer Boundary Layer Measurements During the DOE/VTMX/URBAN Field Experiment in Salt Lake City. In: *Fourth Symposium on Urban Environment* (Norfolk 2002)
- 17.8 N. Matuura, H. Masuda, S. Inuki, S. Kato, S. Fukao, T. Sato, T. Tsuda: Radio acoustic measurement of temperature profile in the troposphere and stratosphere, *Nature* **323**, 426–428 (1986)
- 17.9 G.R. Diak, W.L. Bland, J.R. Mecikalski: A note on first estimates of surface insolation from GOES-8 visible satellite data, *Agricult. For. Meteorol.* **82**, 219–226 (1993)